Flow, Turbulence and Combustion
https://doi.org/10.1007/s10494-019-00065-5

Turbulence and Thermal Structure in the Upper Ocean: Turbulence-Resolving Simulations

Sutanu Sarkar[1] · **Hieu T. Pham**[1]

Received: 22 May 2019 / Accepted: 16 August 2019 / Published online: 17 October 2019

Abstract
The upper layer of the ocean participates directly in the exchange of momentum, heat and moisture with the atmosphere. We consider three examples of upper-ocean flow and heat transfer in the present contribution. These examples range from the canonical problem of a stratified shear layer to the surface boundary layer driven by wind and a diurnally varying heat flux to deep cycle turbulence in the Equatorial UnderCurrents (EUC). These problems illustrate stratified shear flow turbulence, wind-driven entrainment in a stratified, rotating fluid, and the communication of surface forcing to subsurface currents in the upper ocean. We discuss the three cases by including new simulations as well as some of our previous work. Direct numerical simulation (DNS) is our tool for the canonical shear layer and, for the other problems, our tool is large eddy simulation (LES) which is increasingly being used to examine turbulent transport and mixing in the ocean. We discuss how buoyancy and rotation affects the spatial structure and temporal evolution of turbulent fluxes, and thereby the distribution of surface inputs of momentum and heat in the upper ocean.

Keywords Turbulence simulation · Stratified turbulence · Ocean turbulence

1 Introduction

The properties of the upper ocean are crucial to weather and climate. The fueling of hurricanes by the tropical ocean, the patterns of the monsoon, and the sea breeze are familiar examples in the realm of weather. The upper ocean responds to wind forcing, the diurnal cycle of surface heating/cooling, rain events and river inflows, and determines the feedback to the atmosphere. It is not possible to understand or predict this response of the upper ocean without knowledge of the turbulent mixing of momentum, heat and salinity. The upper ocean boundary layer (OBL) has a generic structure in the vertical (z): a thin surface skin

✉ Sutanu Sarkar
sarkar@ucsd.edu

Hieu T. Pham
h8pham@ucsd.edu

[1] Mechanical and Aerospace Engineering, University of California at San Diego, 9500 Gilman Drive, La Jolla, CA 92093, USA

with gradients corresponding to the surface air-sea flux, a mixed layer (where stratification is weak and the mean shear is small), and a transition layer with intensified stratification and shear where properties transition to those at the interior. Stratification is thus a key control on ocean mixing and, when the boundary layer response is considered over a time scale larger than a few hours, rotation is also important.

The various processes that lead to upper-ocean mixing include night-time cooling, wind-driven shear, breaking surface waves and Langmuir cells. Turbulence is produced in these processes by enhancing shear or by creating unstable density variation. Most numerical simulations of the upper ocean have used turbulence parameterizations. However, during the past decade, there has been an increase in turbulence-resolving process studies using DNS or high-resolution LES.

In the present paper, we focus on three of our recent studies. The discussion of simulation results starts in Section 2 with the problem of a localized turbulent free shear layer (mixing layer) that develops in a uniformly stratified background. This is a canonical problem of relevance to the general topic of environmental turbulence and serves as an excellent introduction to the competition between shear that promotes turbulence and stratification that suppresses it because complexities involving boundaries, surface forcing, and rotation are excluded. In the typical two-layer configuration [1, 2], inflectional velocity and density profiles with constant velocity and density difference are considered. We consider the related problem of an inflectional velocity profile in a background with uniform and continuous stratification that was simulated to study internal waves radiated by the shear layer [3] and to examine turbulence properties [4]. Results from new simulations conducted at higher Reynolds number (Re) than in our previous work, are presented in Section 2 with a focus on the anatomy of turbulence, its energetics, and the associated scalar mixing. The results are also contrasted with recent high-Re simulations of the two-layer configuration.

In Section 3 we turn to a problem involving heat uptake in the OBL. The thickness and temperature of the OBL depends on the surface heat flux, the wind speed and the entrainment of typically colder subsurface water. The diurnal variability of the surface heat flux - cooling flux in the night and heating in the day - leads to the so-called diurnal warm layer (DWL) whose flow and thermal structure exhibit a diurnal cycle. The diurnal cycle of shear and stratification [5–9] has been quantified through observations and some of the later studies have measured turbulence in the DWL. Owing to its increased daytime stability, the DWL tends to decouple from the subsurface water so that the turbulence below the DWL decreases [5]. Concurrently, the DWL traps the momentum input by the wind and develops a surface jet, the so-called diurnal jet [8]. The diurnal stratified jet could support shear-driven turbulence if the local Ri is sufficiently small, $Ri < 0.25$. Recent measurements [6, 7, 9] indicate that turbulence is enhanced in the diurnal jet. High-resolution simulations have not investigated the DWL, thus motivating the present LES.

Section 4 concerns a problem in the equatorial ocean. Near the equator, a current with vertical shear is maintained by the easterly trade winds. These tend to accelerate a westward flow at the surface, which in turn generates a pressure gradient that drives a return flow at depth and the combined flow is the so-called Equatorial Undercurrents (EUC). Stratification is maintained by the combined action of solar heating near the surface and upwelling of cold water at depth, resulting in a pycnocline that coincides roughly with the EUC. Rotational effects on the boundary layer are weak at the equator where $f = 0$. A surprising discovery in the EUC [10, 11] was the existence of turbulence in the stably stratified fluid below the diurnal mixed layer (DML). The turbulence, called deep cycle (DC) turbulence, has a diurnal cycle suggesting that turbulence is triggered by surface fluxes even though it is found deep below the DML. Because it coincides with strong thermal stratification, DC turbulence

has the potential to drive an intense heat flux, thereby establishing a thermal link between the DML and the ocean interior. Mooring records [12] show that, on the seasonal time scale, turbulence exhibits a cycle that is causally connected with the seasonal cycle of sea surface temperature (SST). To understand the seasonality of EUC turbulence, we have performed LES using realistic surface forcing as well as initial velocity and temperature profiles based on field observations. In Section 4, we present highlights of the flow structure reported by Pham et al. [13] and also present new LES results regarding the thermal transport.

In all three problems, the intial configuration develops flow patterns that lead to instability and ultimately turbulence. The stability of a fluid layer at rest depends on the vertical (z) variation of potential density which differs from that of the density because of the compressibility, albeit small, of water. The potential density, ρ_p, increases with salinity (S) and decreases with temperature (T). The buoyancy is defined by $b = -g(\rho_p - \rho_0)/\rho_0$ and the stratification is measured by the squared buoyancy frequency defined by $N^2 = db/dz$. The oceanic background is typically stable and N^2 is a positive quantity. A flow might lead to a region with locally negative N^2 which is susceptible to convective instability and ultimately turbulence. An example is the convective instability during the breaking of surface waves and internal gravity waves. A central parameter governing turbulence in a stratified shear flow is the gradient Richardson number $Ri = N^2/S^2$, where S^2 is the square of the vertical shear, $\partial U/\partial z$, of the mean horizontal current. Linear stability analysis suggests that $Ri < 1/4$ is a necessary condition for instability growth in the geophysically relevant limit of high Reynolds number Re [14, 15].

2 Stratified Shear Layer

We perform direct numerical simulations (DNS) of a shear layer in a linearly stratified environment to investigate the competition between destabilizing shear and stabilizing stratification on the flow evolution. The shear layer has a depth-varying velocity profile, $U(z)$, with a velocity jump, ΔU, over a thickness, δ:

$$U(z) = \frac{-\Delta U}{2} \tanh(\frac{2z}{\delta}). \tag{1}$$

The density at $t = 0$ is set to the background density profile, $\rho_b(z)$, with a constant gradient:

$$\rho_b(z) = \rho_0 - \frac{\rho_0 N_0^2}{g} z, \tag{2}$$

where N_0^2 is the squared buoyancy frequency of the ambient. The initial velocity and density are set according to Eqs. 1 and 2, respectively. Small-amplitude broadband velocity fluctuations are superposed on the mean to initiate shear instability.

The Navier-Stokes equations under the Boussinesq approximation are advanced in time to solve for the three velocity components (u, v, w), the density deviation ($\tilde{\rho}$) and the dynamic pressure (p). The non-dimensional form of the equations is as follows:

$$\begin{aligned} \frac{\partial u_i}{\partial x_i} &= 0, \\ \frac{\partial u_i}{\partial t} + \frac{\partial (u_j u_i)}{\partial x_j} &= -\frac{\partial p}{\partial x_i} - Ri_0 \tilde{\rho} g_i + \frac{1}{Re} \frac{\partial^2 u_i}{\partial x_j \partial x_j}, \\ \frac{\partial \tilde{\rho}}{\partial t} + \frac{\partial (u_j \tilde{\rho})}{\partial x_j} &= \frac{1}{RePr} \frac{\partial^2 \tilde{\rho}}{\partial x_j \partial x_j} - w \frac{d\rho_b}{dz}, \end{aligned} \tag{3}$$

where $\tilde{\rho} = \rho - \rho_b$, $Re = \Delta U \delta / \nu$ is the Reynolds number, $Pr = \nu/\kappa$ is the Prandtl number, and $Ri_0 = N_0^2 \delta^2 / \Delta U^2$ is the gradient Richardson number at z = 0 at the initial time. The material properties, ν and κ, are molecular values of viscosity and thermal diffusivity of water, respectively, while g_i is the gravity vector. The simulation has $Re = 24,000$, $Pr = 1$, and $Ri_0 = 0.12$. The gradient Richardson number ($Ri(z) = N^2/S^2$) is 0.12 at the center of the shear layer, a value that is smaller than the critical value of 0.25 and, therefore, the shear layer is susceptible to Kelvin-Helmholtz (K-H) shear instability. Here, $S = d\langle u \rangle / dz$ is the vertical shear where the angle brackets are used to denote mean values, obtained by horizontal averages. In subsequent discussion, we use primes to denote fluctuation quantities, the deviations from the horizontal mean.

The computational domain is a rectangular box with $L_x = 11.52\delta$, $L_y = 5.76\delta$, and $L_z = 30\delta$ discretized using a grid size of $1536 \times 768 \times 1024$ (≈ 1.2 billion grid points). The grid is uniform in x and y directions with a grid spacing of 0.0075δ. The vertical grid spacing of 0.0075δ is deployed in the region $-2.5 \leq z \leq 2.5$; the grid is stretched at a rate of 3% outside this region. Periodic boundary conditions are applied in the horizontal directions while free slip conditions are used at the top and bottom boundaries. Sponge layers are set up in the regions with $|z| > 10\delta$ to prevent reflection of internal waves from the boundaries. To implement the sponge layer, forcing terms, $\phi(z)$, are added to the right-hand-side of the momentum and density equations, Eq. 3:

$$-\phi(z)\left[u_i(x_i,t) - u_{i,\infty}\right], \quad -\phi(z)\left[\rho(x_i,t) - \rho_\infty\right]. \tag{4}$$

Here, $u_{i,\infty}$ and ρ_∞ are the initial velocity and density values at the boundaries. The damping function, $\phi(z)$, increases quadratically from $\phi = 0$ at $|z| = 10$ to $\phi = 0.165$ at the top and bottom boundaries.

Due to the weak stratification and strong shear, the K-H instability develops as growing waves in the velocity and density perturbations. The perturbations grow to finite amplitude and form multiple billows connected together by thin braids. The billows exchange water vertically (overturn the density field) as illustrated in Fig. 1a at time $N_0 t = 40$. Heavy fluid below the center of shear layer is transported upward and causes the water on the top to be heavier. In contrast, light fluid above the center of the shear layer is pushed downward and, as a result, the water below the center becomes lighter. As the billows grow in size and the braids become thinner, the local shear rate in the billows is enhanced and *secondary* instabilities grow along the outer periphery of the billows and along the braids. Small-scale but coherent vorticity structures develop at the bottom boundary of the middle billow at $x \approx 7.6\delta$ in Fig. 1b as well as along the braid in the region $8\delta \leq x \leq 11\delta$. These secondary instabilities result in strong localized mixing as indicated by the elevated dissipation rate and scalar dissipation rate in Fig. 1c, d, respectively. In Fig. 1c–d, the dissipation rate (ε) is defined by Eq. 7 and the scalar dissipation rate (χ_ρ) is defined by $\chi_\rho = 2\kappa \langle \partial\rho'/\partial x_j \partial\rho'/\partial x_j \rangle$. It is important to note that, during the transition to turbulence (e.g. $N_0 t = 40$), the turbulent mixing is stronger at the outer edge of the billows and along the braids. The dissipation rate in the core of the billows is many orders of magnitude weaker. The secondary instabilities break down the billows into three-dimensional turbulence at a later time $N_0 t = 47$ as shown in the panels on the right column of Fig. 1. The turbulence is more homogenous and spreads throughout the shear layer at this time. It is noted that the strongest peak dissipation rate occurs at $N_0 t = 40$, i.e. during the onset of the secondary instabilities. We note the secondary instabilities and turbulence have significantly spanwise variability as shown in Fig. 2, and the instabilities are driven by both shear and convection similar to the two-layer problem at high Re [16]. When the shear layer has a more homogeneous distribution of turbulence at $N_o t = 47$, the patches with

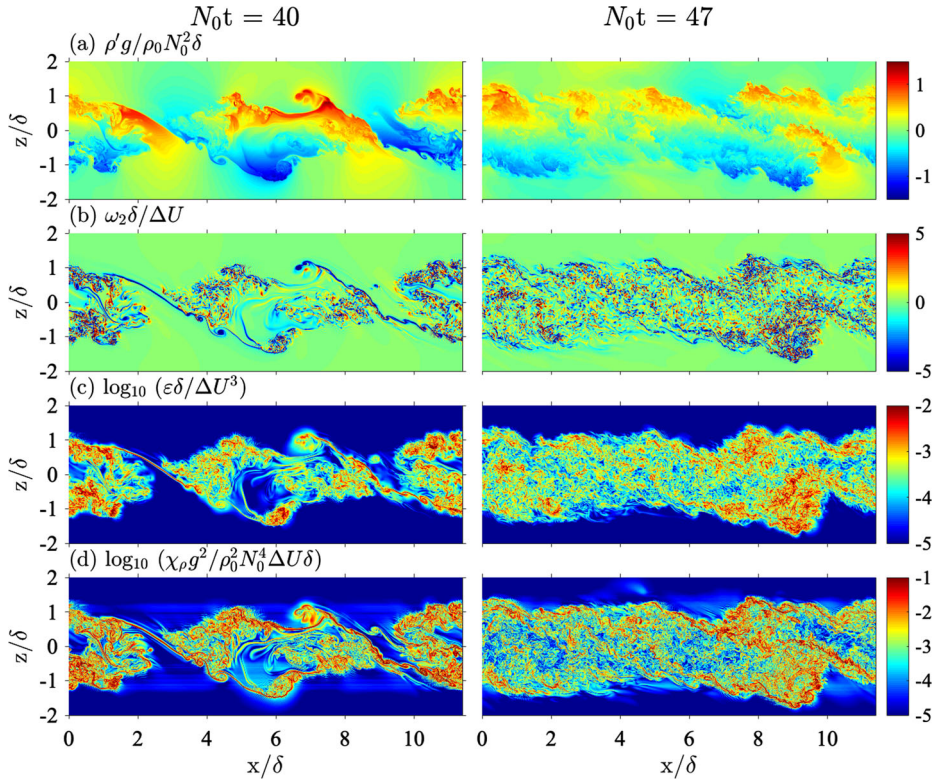

Fig. 1 Anatomy of mixing during the transition from Kelvin-Helmholtz shear instability to three-dimensional turbulence through snapshots of **a** density perturbation, ρ'; **b** spanwise vorticity, ω_2; **c** dissipation, ε; and **d** scalar dissipation, χ_ρ. The panels on the left column shows the patches of intense mixing due to the secondary instabilities at time $N_0 t = 40$ while the ones on the right column depict a more homogeneous turbulence field at time $N_0 t = 47$

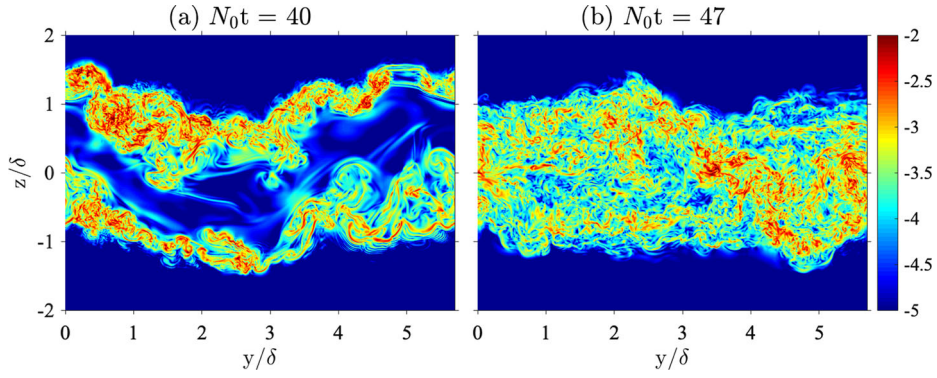

Fig. 2 Snapshots of non-dimensional dissipation rate in log scale, $\log_{10}(\varepsilon\delta/\Delta U^3)$, through the core of a K-H billow at $x = 7.6\delta$ show the spanwise variability of secondary instabilities and turbulence at times: **a** $N_0 t = 40$; and **b** $N_0 t = 47$

large dissipation that were seen at $N_0t = 40$ are less prevalent and, as will be shown, the volume-integrated dissipation is also somewhat smaller than at $N_0t = 40$.

The evolution of the shear layer can be divided into four distinct stages as illustrated with the temporal evolution of the squared shear S^2, the stratification N^2 and the gradient Richardson number, $Ri = N^2/S^2$, shown in Fig. 3a–c, respectively. During the first stage, $N_0t < 20$, the K-H instability slowly develop from infinitesimal perturbations by extracting energy from mean kinetic energy, and thus, S^2 and N^2 gradually decrease at the center of the shear layer. The Richardson number, initially smaller than the critical value of 0.25 [14], gradually increases. During the second stage, $20 \leq N_0t \leq 35$, the finite-amplitude K-H waves develop into K-H billows while N^2 and S^2 at z = 0 are significantly reduced due to the vertical exchange of momentum and density associated with the enlargement of the billows. Thin outer transition layers of enhanced N^2, S^2 and Ri develop at the top and bottom boundaries of the shear layer to separate the billows from non-turbulent fluid in the ambient. The gradient Richardson number shows peaks at these outer transition layers with values exceeding unity. During the third stage, $35 \leq N_0t \leq 45$, the billows break down into three-dimensional turbulence by secondary instabilities with spanwise variability. Due to the strong turbulence, N^2 and S^2 at z = 0 abruptly decrease while Ri continues to increase. The outer transition layers that developed during the second stage are also eroded by the turbulence; N^2 and S^2 decrease as the layers thicken considerably. Toward the end of the third stage, Ri at z = 0 increases rapidly and a central internal transition layer forms. The

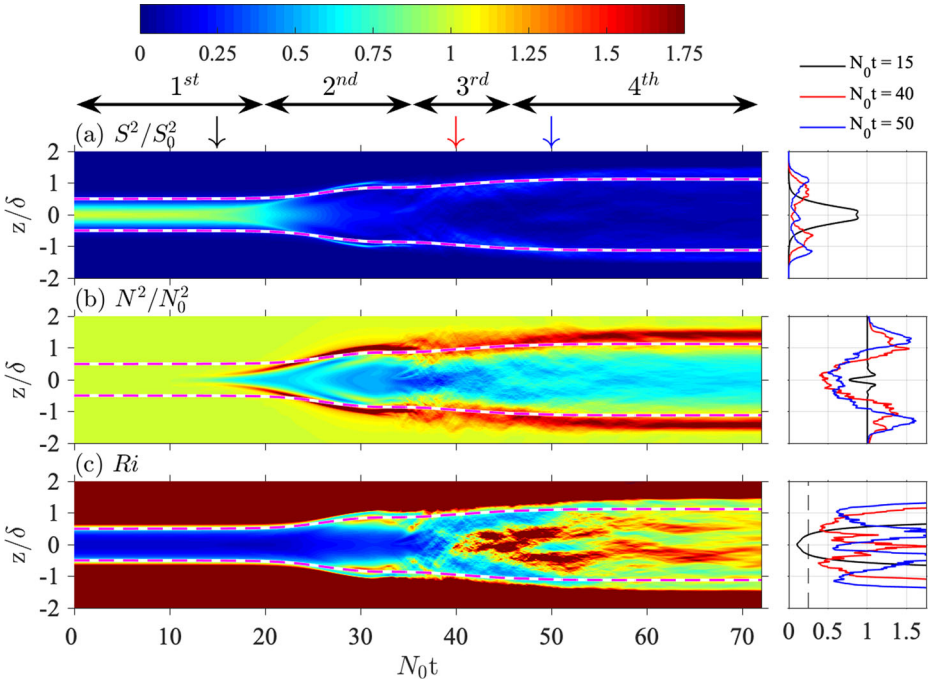

Fig. 3 Variability of **a** squared shear, S^2; **b** squared buoyancy frequency, N^2; and **c** gradient Richardson number, Ri during four stages of the evolution of the stratified shear layer. The right panel of each subfigure shows vertical profiles of the variables at three different times marked by vertical arrows ($N_0t = 15$, $N_0t = 40$, and $N_0t = 50$). The two dashed lines in **a**–**c** mark the edges of the shear layer at $\pm 2\delta_\theta$. The dashed vertical line in the right panel of (**c**) marks the critical value of $Ri = 0.25$

inner transition layer (as will become clearer when mean profiles are discussed) is the region between a thin central region with weak shear and turbulence that is sandwiched between outer layers with stronger shear and turbulence. Finally, turbulence decays during the last stage, $N_0 t > 45$ in which Ri over the entire shear layer gradually changes due to molecular diffusion.

The vertical profiles of N^2 and S^2 shown in the right panels of Fig. 3a, b indicate that, when the turbulence is locally strong at z = 0, both N^2 and S^2 are reduced at this depth but they are enhanced in the regions above and below (compare the profiles between $N_0 t = 15$ and 40). When the billows break down by secondary instabilities during the second stage, the vertical profiles of S^2 and N^2 exhibit *double shear layers* with enhanced stratification that are separated by a zero-shear weak-stratification layer at z = 0. Subsequently, the double shear layers become turbulent so that the turbulent mixing in the regions above and below z = 0 become stronger than that at z = 0. The shear and the stratification increase (compare N^2 and S^2 at z = 0 between $Nt = 40$ and 50 in Fig. 3a,b) to form an internal transition layer between the double shear layers. The internal transition layer persists for a short period of time, $45 \leq N_0 t \leq 55$, after which it is eroded by the turbulence above and below in the double shear layers. The double layers of stratified shear at $z/\delta \approx \pm 1.2$ become a permanent structure; they persist long after the turbulence completely decays at all depths.

Among the four stages, the shear layer thickness grows considerably faster during the second and third stages. The dashed lines in Fig. 3 mark the upper and lower edges of the shear layer, $z_e = \pm 2\delta_\theta$, where δ_θ is momentum thickness defined as follows:

$$\delta_\theta = \int_{-10\delta}^{10\delta} \left(\frac{1}{2} - \langle u \rangle\right)\left(\frac{1}{2} + \langle u \rangle\right) dz\,. \tag{5}$$

The fastest growth of δ_θ occurs in the second stage during which the billows enlarge. As the billows break down, turbulence inside the double shear layers entrains external fluid into the shear layer making the thickness grow further. During the last stage, the momentum thickness ceases to grow.

The asymptotic late-time value of δ_θ, normalized by its initial value, is found to vary considerably with the initial Richardson number Ri_0. Watanabe et al. [17] show that, as Ri_0 increases from 0.01 to 0.08, the asymptotic value of $\delta_\theta/\delta_{\theta,0}$ decreases from about 5.6 to 2.4 at a Reynolds number, $Re = 6,000$. They also find that increasing the Reynolds number slightly reduces the asymptotic values of δ_θ. The asymptotic value of $\delta_\theta/\delta_{\theta,0}$ in the present simulation is approximately 2.24 which is smaller than the values reported in Watanabe et al. [17] due to the stronger stratification of $Ri_0 = 0.12$ and, possibly, the larger Reynolds number, $Re = 24,000$. Another parameter typically used to describe the shear layer between two layers of fluid with different density is the bulk Richardson number, $Ri_b = 4\Delta\rho g \delta_\theta/\rho_0 \Delta U^2$, where $\Delta\rho$ and ΔU are the density and velocity difference, respectively, across the shear layer thickness, $4\delta_\theta$. Brucker and Sarkar [18] show that the asymptotic value of Ri_b at late time in the two-layer problem is approximately 0.3 when the value at the initial time is prescribed to take various values between 0.05 and 0.1. In the present simulation, in which the density varies continuously with depth, the bulk Richardson is computed as $Ri_b = 16 N_0^2 \delta_\theta^2/\Delta U^2$ (for equivalence to the two-layer problem), and the asymptotic value of Ri_b is found to be 0.6, twice as large as the values in the two-layer problem reported by Brucker and Sarkar [18]. The larger asymptotic value for Ri_b in the present study suggests that external stratification can play an important role on the net turbulent transport over the lifecycle of a stratified shear layer.

The turbulent kinetic energy (t.k.e) budget can be used to quantify the overall turbulence energetics as the shear layer evolves in time. The budget is defined as follows:

$$\frac{DK}{Dt} = P - \varepsilon + B - \frac{\partial T_3}{\partial z}. \tag{6}$$

Here, the turbulent kinetic energy (K), production (P), dissipation (ε), buoyancy flux (B), and transport term (T_3) are specified as follows:

$$\begin{gathered} K = 1/2\langle u_i' u_i' \rangle, \quad P = -\langle u'w' \rangle \frac{\partial \langle u \rangle}{\partial z}, \quad \varepsilon = \frac{2}{Re_0} \langle S_{ij}' S_{ij}' \rangle, \quad S_{ij}' = \frac{1}{2}\left(\frac{\partial u_i'}{\partial x_j} + \frac{\partial u_j'}{\partial x_i}\right), \\ B = -Ri_0 \langle \rho' w' \rangle, \quad T_3 = \frac{1}{2}\langle w' u_i' u_i' \rangle + \frac{1}{\rho_0}\langle w' p' \rangle - \frac{2}{Re_0}\langle u_i' S_{3i}' \rangle \end{gathered} \tag{7}$$

The $t.k.e$ budget integrated from $z = -5\delta$ to 5δ shown in Fig. 4a indicates that the largest gain of the $t.k.e$ in the shear layer occurs during the second stage of the evolution. The positive dK/dt is supported by the positive shear production. The buoyancy flux is negative, i.e., there is a gain in the available turbulent potential energy too. The peak turbulent mixing of momentum as indicated by ε occurs during the third stage when the positive production is balanced by the dissipation and the buoyancy flux with the former being the larger sink of $t.k.e$. The double peaks in the production during the second and third stages emphasize two different regimes of $t.k.e$.. The rise of P during the second stage is predominantly driven by coherent, narrow-band, low-mode, wave-like instabilities. The dissipation rate is

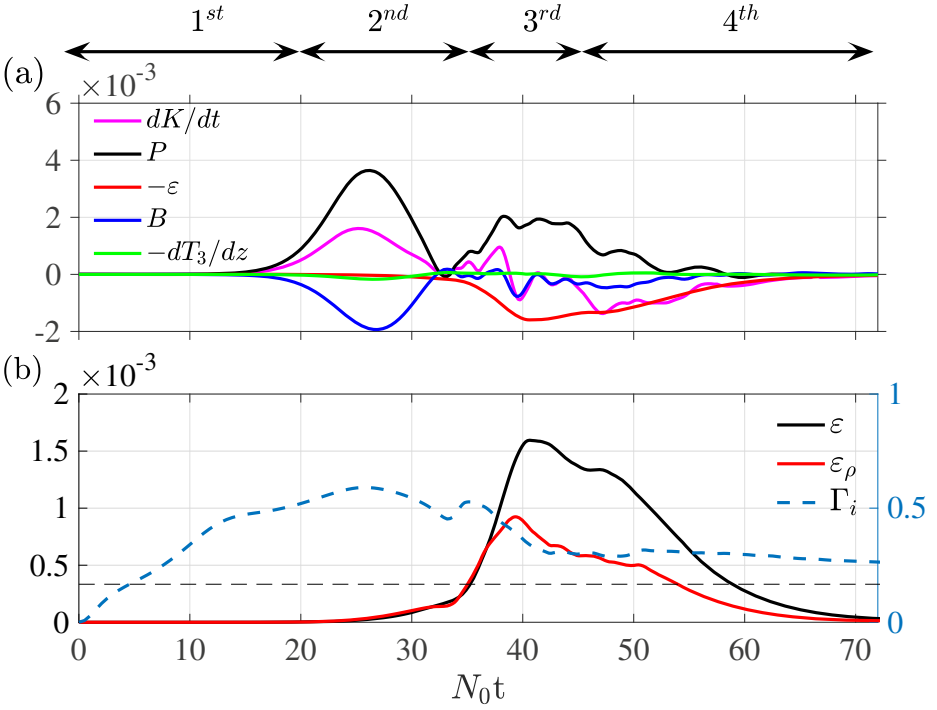

Fig. 4 Evolution of (**a**) TKE budget integrated over the shear layer, $-5 < z/\delta < 5$; and **b** mixing efficiency, $\Gamma_i = \varepsilon_\rho/(\varepsilon + \varepsilon_\rho)$, where ε_ρ is the scalar dissipation. The budget terms in (**a**) are non-dimensionalized by ΔU^3

insignificant at this time due to the lack of energy in high modes. In contrast, broadband turbulence dominates the shear layer as the production resurrects during the third stage and, at this time, there is a significant amount of dissipation, negative buoyancy flux, and scalar dissipation. The production during the second stage stirs the density in the shear layer while the production during the third stage mixes the density gradients that were formed during the second stage. To summarize, turbulent kinetic energy is extracted at the low mode, i.e., the size of the billows, and cascades to higher modes through a series of secondary instabilities to give rise to broadband turbulence and mixing.

Of interest is how much scalar mixing does turbulence lead to? Scalar mixing is quantified through the dissipation rate of turbulent potential energy, ε_ρ, defined as follows:

$$\varepsilon_\rho = \frac{1}{PrRe}\frac{g}{\rho_0 \partial\rho_b/\partial z}\left\langle \frac{\partial\rho'}{\partial x_i}\frac{\partial\rho'}{\partial x_i}\right\rangle. \tag{8}$$

Figure 4b indicates that ε_ρ evolves hand-in-hand with the dissipation (ε) of $t.k.e$. The mixing of the density field is predominantly driven by the broadband turbulence during the third stage of the evolution of the shear layer. There is substantial stirring during the second stage, but not much mixing. Stirring is not irreversible molecular mixing since some of the gain in the available potential energy can feed back into the kinetic energy while mixing is a permanent gain in the background potential energy [1, 19]. To parameterize the rate of turbulent mixing, ocean modelers typically rely on the mixing efficiency, $\Gamma = \varepsilon_\rho/(\varepsilon + \varepsilon_\rho)$, to obtain eddy diffusivity K_ρ through the relation $K_\rho = \Gamma\varepsilon/N^2$ and a typical value of $\Gamma = 1/6$ is used in the ocean modeling community [20–22]. Figure 4 shows that the mixing efficiency ($\Gamma_i(t)$ computed using vertically-integrated values of ε and ε_ρ) in the shear layer is generally higher than this value of 1/6. The high values of mixing efficiency during the first and second stages indicate that the mixing by the K-H waves and coherent billows is far more efficient than the mixing by the broadband, dissipative turbulence during the other two stages. The mixing efficiency reaches values as high as 0.6 at the beginning of the third stage and it then decreases toward the value of 0.25 at the end of the fourth stage. Since Γ_i varies significantly over the four stages, we compute the cumulative mixing efficiency, Γ_c, by integrating the scalar dissipation and dissipation over the four stages before taking the ratio and obtain $\Gamma_c = 0.34$ or $\varepsilon_\rho/\varepsilon = 0.52$. Thus, the amount of energy expended to mix the scalar field is 0.63 times the amount used to mix the momentum field. This value of 0.52 is also comparable to the value of the bulk Richard number, $Ri_b = 16N_0^2\delta_\theta^2/\Delta U^2 = 0.6$, at the end of the fourth stage.

The mixing efficiency (Γ_c) is sensitive to the Reynolds number, Prandtl number, Richardson number, and even the type of vertical shear instabilities [23–25]. The mixing efficiency is found to be smaller at low Re, approximately 0.31 for Re = 1,280 and 5,000 and $Ri_0 = 0.05$ [3, 4]. The mixing efficiency increases to 0.39 at Re = 24,000 and $Ri_0 = 0.12$, the parameters of the present simulation. At a low Reynolds number, the nature of the secondary instabilities is different and alters the transition from K-H instability to turbulence. The transition to turbulence at lower Reynolds number is dominated by convective turbulence in the core of the billow, not the secondary instabilities at the edges of the billows. While there are only a few studies which focus on Γ of a shear layer in a continuously-stratified background as in the present simulation, mixing efficiency in two-layer shear flow has been widely reported. In this type of flow, Mashayek and Peltier [23] finds that Γ can be as high as 0.45 at Re = 40,000, Pr = 1 and $Ri_0 = 0.12$ while Salehipour et al. [26] find that, at Re = 24,000 and $Ri_0 = 0.12$, Γ decreases from approximately 0.23 to 0.18 as the Prandtl

number increases from 1 to 16. Recent simulations of Kaminski and Smyth [27] show that, for Re = 4,000 - 16,000 and $Ri_0 = 0.12 - 0.2$, the mixing efficiency can be as small as 0.1 when there is a sufficiently strong field of pre-existing turbulence in the shear layer. The pre-existing turbulence prevents the growth of the pre-turbulent billows and, therefore, the mixing efficiency is smaller.

3 Diurnal Warm Layer

The thickness and temperature of the upper-ocean boundary layer depends on the surface heat flux, the wind speed and the entrainment of typically colder subsurface water. The diurnally varying solar insolation leads to the so-called diurnal warm layer (DWL) which is a surface layer whose physical properties, including turbulence, exhibit diurnal modulation. During the day, solar insolation can substantially increase the temperature of the wind-driven boundary layer and increase the near-surface stratification, an effect that is particularly significant when the solar flux is strong as in the tropical and subtropical oceans and under conditions of calm-to-moderate wind. During the night, the near-surface stratification relaxes and there is onset of convection. The diurnal cycle of shear and stratification [5–9] has been quantified through observations and some of the later studies have measured turbulence in the DWL. High-resolution simulations have not examined the DWL motivating the present LES.

A westward wind in the negative x direction is imposed with stress $\tau_w = -0.06$ N m^{-2}, which corresponds to moderate wind. There is an initial spinup of 15 hrs. At the start of the spinup, the temperature is uniform at $T = 25°C$ over the entire domain depth. The salinity (S) has the following nonuniform distribution: S is constant over a surface layer of 20 m and then increases linearly in an interior with constant $N^2 = -g/\rho_0 d\rho/dz = 10^{-4}$ s^{-2}. At the end of the 15 hr period, when a mixed layer of wind-driven turbulence with thickness $h_0 = 20$ m has formed, a diurnally varying heat flux and the Coriolis rotation effect are applied, and the DWL simulation starts (time is reset to $t = 0$). The Coriolis parameter $f = 4.5 \times 10^{-5}$s^{-1} corresponds to $18°N$, a location in the Northern Bay of Bengal. The heat flux has a constant non-solar cooling component of $Q_{ns} = 150$ Wm^{-2} and a diurnal cycle of solar heat flux with a peak of $Q_s = -827$ Wm^{-2} (negative implies downward heat flux). The diurnal variation of surface temperature is much less on the ocean than on land. Therefore, the assumption of constant Q_{ns} is a reasonable approximation. The surface forcing corresponds to a net daily warming heat flux of $Q = -95$ Wm^{-2} that creates the diurnal warm layer (DWL) capped by the salt-stratified halocline. The objective is to understand how the diurnal variability modulates turbulence and thus the space-time redistribution into the ocean of the surface heat input. The simulation is conducted over a period of 7 days. Table 1 gives important parameters of the simulations.

3.1 Numerical model

A right-handed coordinate system with x pointing to the east, y pointing north, and z pointing up is used. The equation of state for density is approximated as a linear function of temperature and salinity:

$$\rho = \rho_0 - \alpha(\theta - \theta_0) + \beta(S - S_0) \,, \tag{9}$$

Table 1 Parameters used in the LES of the diurnal warm layer

dS/dz (psu m^{-1})	N_0^2 (s^{-2})	N_0/f	h_* (m)	L_O (m)	Re_N	L_x, L_y (m)	L_z (m)
–0.0127	1×10^{-4}	222	0.76	–3.44 –15.52	5,837	64	83

dS/dz is the constant vertical salinity gradient in the interior, and N_0/f measures the strength of stratification (buoyancy frequency N) with respect to the rotation rate f. The stable stratification introduces a length scale, $h_* = u_*/N_0$, where u_* is the friction velocity due to the wind stress applied at the ocean surface, and the Reynolds number is $Re_N = u_*^2/\nu N_0$. The surface heat flux introduces the Obukhov length scale, $L_O = -\rho_0 c_p u_*^3/\kappa\alpha g(Q_s + Q_{ns})$, which varies from its maximum magnitude of −15.52 m in the night to its maximum of 3.44 m at daytime. L_x, L_y and L_z are the streamwise, spanwise, and vertical grid domain sizes, respectively. The simulations are performed with $Sc = 700$ for salt diffusion and $Pr = 7$ for temperature diffusion in water

where $\alpha = 2 \times 10^{-4}\,^\circ C^{-1}$ and $\beta = 8 \times 10^{-4}\,\text{psu}^{-1}$. In LES, the equations of motion involving along-wind (x) velocity $\overline{u}$, cross-wind (y) velocity $\overline{v}$, vertical velocity $\overline{w}$, salinity $\overline{S}$, and temperature $\overline{T}$ take the following non-dimensional form:

$$\frac{\partial \overline{u}_j}{\partial x_j} = 0, \tag{10}$$

$$\frac{\partial \overline{u}_i}{\partial t} + \frac{\partial\left(\overline{u}_j\,\overline{u}_i\right)}{\partial x_j} = \frac{-\partial \overline{P}}{\partial x_i} + \epsilon_{ijk}\frac{\overline{u}_j f \delta_{k3}}{N_0} + \frac{1}{Re_b}\frac{\partial^2 \overline{u}_i}{\partial x_j \partial x_j} + \overline{b}\delta_{i3} - \frac{\partial \overline{\tau}_{ij}}{\partial x_j}, \tag{11}$$

$$\frac{\partial \overline{S}}{\partial t} + \frac{\partial\left(\overline{u}_j \overline{S}\right)}{\partial x_j} = \frac{1}{Re_b Sc}\frac{\partial^2 \overline{S}}{\partial x_j \partial x_j} - \frac{\partial \overline{Q_j^S}}{\partial x_j}, \tag{12}$$

$$\frac{\partial \overline{T}}{\partial t} + \frac{\partial\left(\overline{u}_j \overline{T}\right)}{\partial x_j} = \frac{1}{Re_b Pr}\frac{\partial^2 \overline{T}}{\partial x_j \partial x_j} - \frac{\partial \overline{Q}_j}{\partial x_j} - \frac{\partial Q_{sw}}{\partial z}, \tag{13}$$

where the overbar denotes filtered quantities, g denotes gravity acting in the vertical direction, $b = -g(\rho/\rho_0 - 1)$ is the buoyancy, and $f = 2\Omega \sin\theta$ where Ω is the angular velocity of earth's rotation and θ is the latitude. The subgrid stresses $\overline{\tau}_{ij}$, the subgrid heat flux $\overline{Q}_j$, and the subgrid salinity flux $\overline{Q_j^S}$ are modeled in the LES. The variables in these equations have been normalized by the characteristic velocity scale u_*, the characteristic buoyancy length scale $h_N = u_*/N_0$, and the characteristic buoyancy scale $N_0 u_*$. The governing equations contain four non-dimensional parameters: Reynolds number $Re_b = u_*^2/\nu N_0$ where ν is the molecular viscosity; the ratio N_0/f between stratification and rotation parameters; the Schmidt number $Sc = \nu/\kappa_s$ where κ_S is the diffusivity of salt in water; and, the Prandtl number $Pr = \nu/\kappa_T$ where κ_T is the diffusivity of temperature in water. To ease the notation used to discuss in the following sections, the overbar denoting filtered quantities is omitted.

Surface boundary conditions are based on typical fluxes of momentum and heat observed at the sea surface. The momentum flux, τ_w, and the nonsolar heat flux, Q_{ns}, are applied as surface boundary conditions on velocity and temperature, respectively. The diurnally-varying solar heat flux, Q_{sw}, is applied as a time- and depth-varying forcing term in the temperature (13): $Q_{sw} = Q_s(t)\,Tr(z)$. The solar flux at the surface, $Q_s(t)$, is given in Fig. 6a. The strongest solar flux (most negative) value of $Q_s = -827\,W\,m^{-2}$ occurs at noon and Q_s is zero during night time. The transmissivity, $Tr(z)$, exponentially decays with depth as in the 9-term parameterization of Paulson and Simpson [28] with water type IA [29].

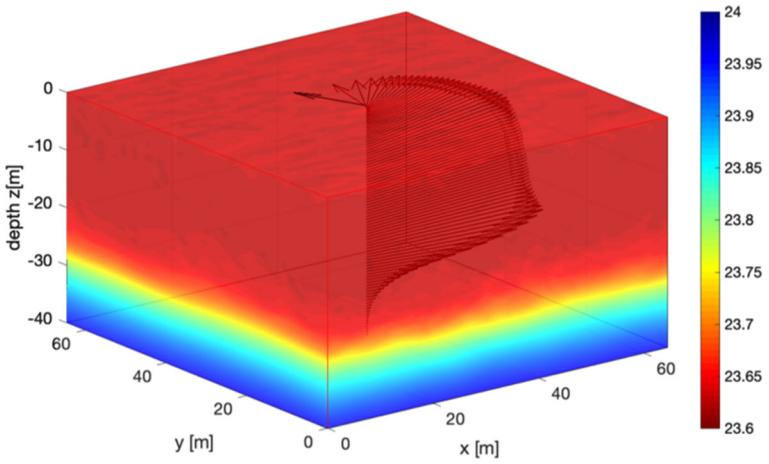

Fig. 5 Visualization of the rotating, stratified OBL that forms when a wind stress and a diurnal heat flux are applied to the upper-ocean surface. Initially, a homogeneous constant-density layer of $h = 20$ m overlies a salt-stratified interior with constant salinity (density) gradient. Perspective of the turbulent density field shown at t = 06:00 hours of the seventh day of the simulation. Vectors show the mean velocity of the rotating current forced by the wind stress applied in the $-x$ direction

The LES uses a structure-function based model [30] to compute the subgrid stress and the subgrid diffusivities for the salinity and temperature fields, and the subgrid Prandtl and Schmidt numbers are taken to be 0.5. The simulations are performed on a computational grid with $N_x = 128$, $N_y = 128$ and $N_z = 256$ points. The domain size is modest; however, the long time (7 days) of the simulation leads to a large computational time. The horizontal grid spacing of 0.5 m is uniform while the vertical grid spacing Δz is nonuniform. The smallest vertical grid spacing of 10 cm is at the surface. The buoyancy length scale, $h_N = u_*/N_0$, that is dynamically important for capturing entrainment is resolved by the grid.

An upper Ekman layer develops in the stratified, rotating fluid that is forced by the wind stress. Rotation imposes a veer on the horizontal velocity that can be seen by the rotation of the velocity vectors in Fig. 5 with increasing depth. The surface velocity has a clockwise veer. The magnitude of the surface veer in the turbulent Ekman layer is smaller than the laminar value of 45°. The velocity profile exhibits two layers: (1) a slab structure near the surface where the cross-wind velocity remains constant, and (2) a spiral structure toward the bottom of the Ekman layer where both along-wind and cross-wind velocities rapidly change with depth. The Ekman layer is capped by the halocline (sharp change in the density owing to a sharp change in salinity) that can be seen in the region between 25 and 30 m in Fig. 5. The halocline marks the bottom of the mixed layer. The MLD increases by entrainment of interior dense fluid across the interface between the mixed layer and the interior.

3.2 Mixed layer thickness without surface heat flux

The dependence of the MLD (h) on the problem parameters is of interest. Here, we define the mixed layer depth (MLD), h, to be the distance from the surface to the depth with maximum stratification, N^2. Consider the simpler problem without surface heat flux. At sufficiently high Re so as to ignore the direct influence of viscosity, the dimensional

parameters that govern the problem are $\{u_*, f, N_0\}$ leading to two independent length scales,

$$h_f = u_*/f \quad \text{and} \quad h_N = u_*/N_0\,. \tag{14}$$

In the absence of stratification, h depends only on h_f and, as per experiments and simulations, $h \approx 0.5h_f = 0.5u_*/f$. However, interior stratification reduces the MLD. Pollard et al. [31] used a slab model to deduce that, under a constant wind stress and an uniform stratification, the mixed layer reaches its maximum depth of $2^{3/4}h_P$ at the time $tf = \pi$ where $h_P = \sqrt{h_f h_N} = u_*/\sqrt{fN_0}$ takes account of both stratification and rotation. In a previous LES study [32], the value of MLD after the initial transient (which is longer than the theoretical prediction) was found to be comparable to the maximum value of Pollard et al. [31] over a wide range of interior stratifications, $19.2 < N_0/f < 605.9$. However, there is a difference: later in time, the mixed layer continues to grow in the LES and quantification of the late-time entrainment becomes important.

A scaling law for the entrainment velocity $u_e = dh/dt$ can be obtained as follows. We conceptualize the problem as a mixed layer of thickness, $h(t)$, and uniform buoyancy, $b_{ML}(t)$, that progressively deepens. Let the entrainment buoyancy flux at the interface between the ML and the stratified fluid be $\langle w'b' \rangle = B_e$. Then,

$$B_e = -u_e \Delta b = -\frac{u_e N_o^2 h}{2}, \tag{15}$$

where the first of Eq. 15 is the definition of u_e and the second of Eq. 15 follows from the intial condition of a layer with constant N_0. To obtain B_e, consider the dominant balance in the turbulent kinetic energy (TKE) equation, i.e., among production ($\mathcal{P}$), dissipation (ε) and buoyancy (B):

$$\mathcal{P} = -\langle u'v' \rangle \frac{\partial \langle u \rangle}{\partial z} - \langle v'w' \rangle \frac{\partial \langle v \rangle}{\partial z} = B + \varepsilon. \tag{16}$$

In the entrainment zone, $\mathcal{P}$ and ε scale as u_*^3/l_e, where u_* is the friction velocity and l_e is a turbulent length scale, yet to be determined. As a result of Eq. 16, we obtain $B_e \sim u_*^3/l_e$.

The vertical sides of the density field in the computational domain (Fig. 5) show the turbulent eddies that develop in the stratified, sheared region in the transition layer between the turbulent Ekman layer and the stratified water below. It can be surmised from Fig. 5 that the interfacial turbulent eddies are much smaller than the MLD (h). Equating the kinetic and potential energy of the overturning motions at the interface leads to $l_e \sim u_*/N_0$ so that it follows that $B_e \sim u_*^3/l_e \sim u_*^2 N_0$. Substitution of this expression for B_e on the LHS of Eq. 15 leads to

$$\frac{u_e}{u_*} = C\frac{u_*}{N_0 h} = 0.049\frac{h_N}{h}\,, \tag{17}$$

where the LES results are used to obtain $C = 0.049$. When the flow is non-rotating, u_e has the same dependence on N_0 as in Eq. 17 but the value of C in the late-time rotating cases studied here is an *order of magnitude* smaller than in the non-rotating case (DNS of Jonker et al. [33] and also our LES of the non-rotating regime). It is worth noting that in cases with heat flux, the entrainment velocity depends on another length scale that is introduced into the problem, i.e., the Obukhov length, L_O, defined by

$$L_O = \frac{-\rho_0 c_p u_*^3}{\kappa \alpha g (Q_s + Q_{ns})}, \tag{18}$$

where $\kappa = 0.4$ is the Von Karman's constant and $c_p = 4,000\,\text{J/kg K}$ is specific heat of seawater.

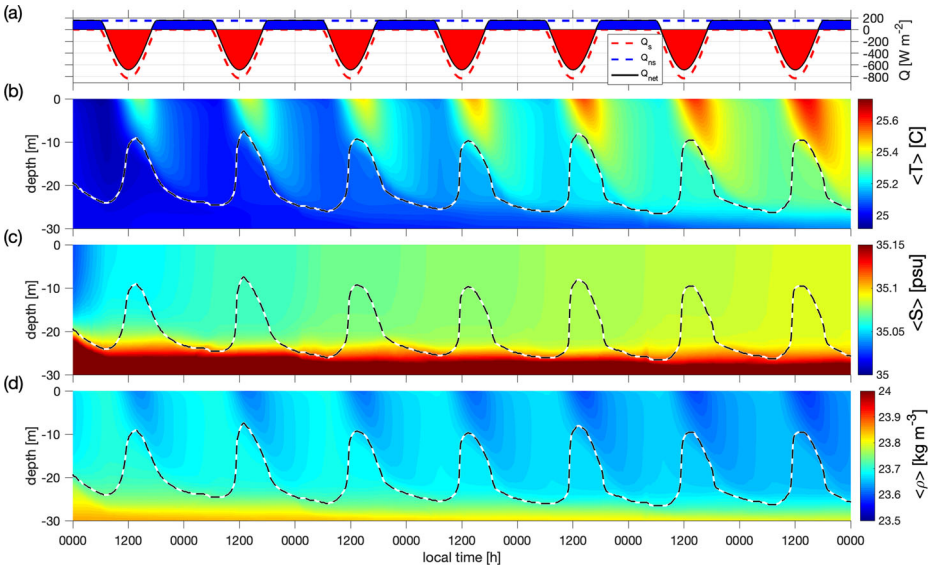

Fig. 6 The variability of DWL physical properties over a week in response of the diurnally varying heat flux shown in the header: **a** components of surface heat fluxes: solar insolation Q_s, non-solar Q_{ns} and net flux, $Q_{net} = Q_s + Q_{ns}$; **b** temperature, **c** salinity, and **d** density. Dashed line in panels (**b**–**d**) shows the MLD

3.3 Diurnal warm layer results

A DWL with variable MLD forms in response to the imposed heat flux with diurnal variability (Fig. 6a). The MLD varies between a peak of approximately 25 m in the night to a minimum of about 10 m a little after the noon-time peak of the heat flux. Here, we define the MLD to be the distance from the surface to the depth at which the density increases by 0.04 kg m^{-3}. The night-time cooling and the daytime heating combine to create a net warming heat flux of $Q = -95$ Wm^{-2}. As a result, the temperature (Fig. 6b) exhibits a secular increase with time in addition to an oscillatory response. The salinity (Fig. 6c) exhibits an increase with time owing to the entrainment of saltier water from below. In spite of the salinity increase, the density (Fig. 6c) decreases with time; evidently, the influence of heat accumulation on mixed-layer density is stronger than that of salt.

The variability of shear and stratification in the DWL is more complex than in the canonical stratified shear layer discussed in Section 2 owing to several factors: a moving stress-driven boundary generates the velocity difference across the stratified layer; the density difference is not imposed by a uniform stratification but has two different causes, namely, a surface heat flux and a salinity jump across the halocline; there is a variable surface heat flux that is cooling at night and warming with a diurnal modulation in the daytime; and, rotation leads to a directional change of the horizontal velocity. After sundown, a surface region of convection with negative N^2 (white regions in Fig. 7b) develops and deepens to approximately 10 m. On the other hand, during daytime, water at 10-m depth stratifies and N^2 increases to $O(10^{-4})$ s^{-2} at noon when the MLD decreases to about 10 m. There is a variability in the shear too. In the canonical stratified Ekman layer without surface heat flux, the shear (S^2) exhibits a monotone decrease with increasing depth until there is an increase of S^2 in the transition layer between the Ekman layer and the capping

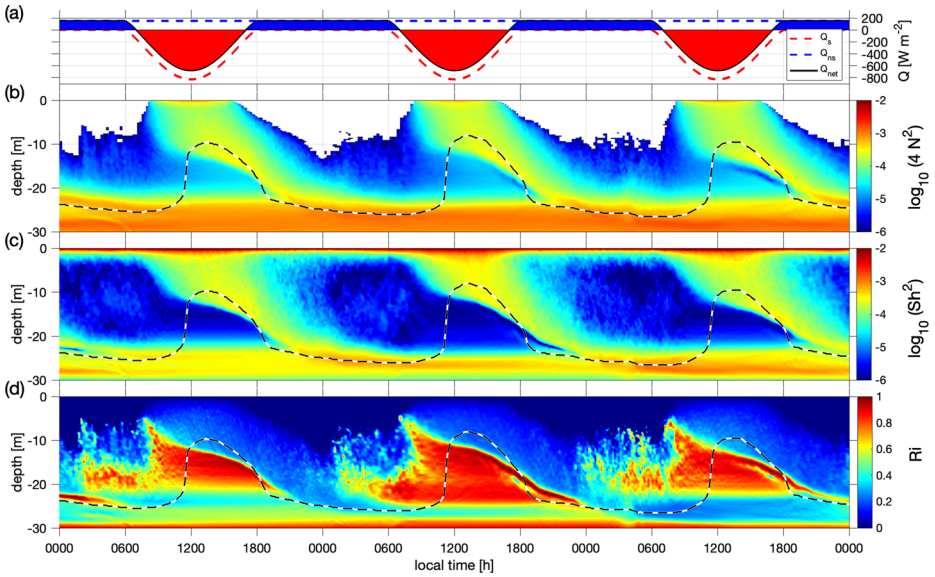

Fig. 7 The mean structure of the stratified and sheared DWL: **a** surface heat fluxes: **b** squared buoyancy frequency, N^2, **c** squared shear, S^2, and **d** gradient Richardson number, Ri. White area in panel (**b**) indicates $N^2 \leq 0$. Dashed line in panels (**b–d**) shows the MLD

stratification below. In the present case (Fig. 7c), nightly convection decreases the squared shear below 2 m to 10^{-6} s^{-2} while, in the day, there is an increase in shear, e.g. at 10-m depth S^2 increases to $O(10^{-4})$ s^{-2}. The region with enhanced shear and stratification that forms as a result of diurnal heating is the so-called *diurnal jet* that has been observed in the upper ocean, e.g. by Price et al. [8], Sutherland et al. [9] and Moulin et al. [7]. In the afternoon, the warming heat flux decreases and so does the shear and stratification at 10-m depth. More interestingly, there is a descending layer of concomitant shear and stratification that tracks the wind-induced deepening of the mixed layer from about 10 m to 25 m as the stabilizing effect of surface heating relaxes. The gradient Richardson number (Ri in Fig. 7d) in the region between 10 and 25 m decreases from larger than 1 to less than the critical value of $Ri = 0.25$ as the descending shear layer passes through. The region encompassed by the diurnal jet and the descending shear layer is in a state of marginal instability with a narrow range of Richardson numbers: $0.15 < Ri < 0.3$.

The modulation of Ri by the diurnally varying heat flux has consequences for turbulence as can be expected from the discussion of the stratified shear layer in Section 2. Ocean observations use the turbulent dissipation rate (ε) as a metric for turbulence; ε is directly measured using turbulent microstructure profilers or is inferred from CTD (conductivity, temperature, and depth) profilers. Night-time dissipation in the LES (Fig. 8b) exhibits a thin (5 m) layer of turbulence with ε as large as $O(10^{-6})$ W kg^{-1} that is driven by boundary-layer shear, while most of the 25-m thick mixed layer exhibits $\varepsilon = O(10^{-7} - 10^{-8})$ W kg^{-1} with the large values associated with intermittent pulses of convective turbulence. After sunrise, convective turbulence rapidly weakens and shuts off within 1 hour after sunrise. The diurnal surface jet begins to form and by 9:00 hrs the layer of ε begins to thicken. The turbulence is driven by the shear of the diurnal jet as can be surmised from the enhanced TKE

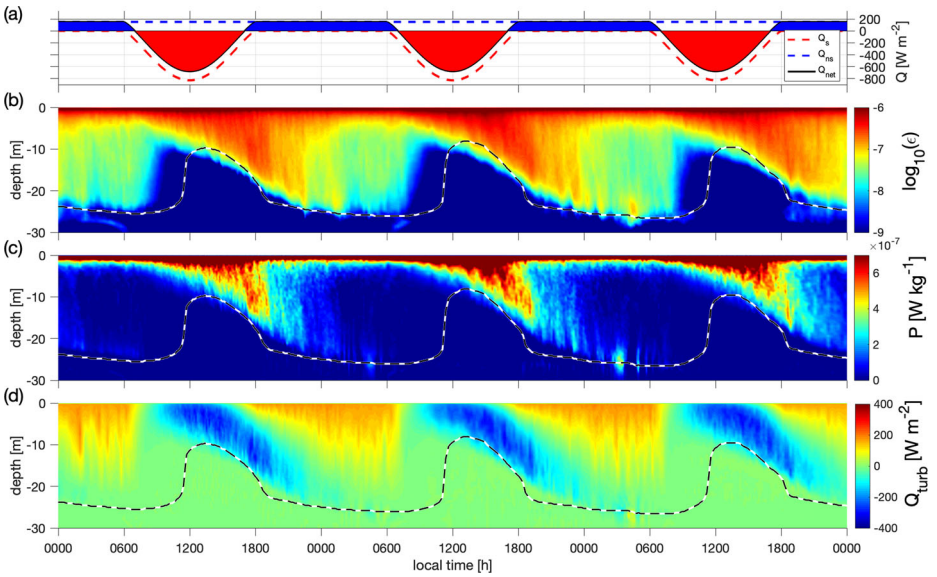

Fig. 8 Turbulence in the DWL: **a** surface heat fluxes; **b** turbulent dissipation rate (ε), **c** turbulent production (P), and **d** turbulent heat flux (Q_{turb}). Dashed line in panels (**b**–**d**) shows the MLD

production (P in Fig. 8c) in the marginally stable region of the diurnal jet that extends down to the location of the descending shear. Owing to the diurnal jet, ε in the region between 10- and 20-m depth increases dramatically in the evening (4:00 - 9:00 hrs) to values near its near-surface maximum of 10^{-6} W kg^{-1}. The turbulent heat flux given by $Q_{turb} = \rho_0 C_p \overline{T'w'}$ is computed and plotted in Fig. 8d. Negative values of Q_{turb} at a vertical location signify warming heat flux. Turbulence associated with the thickening diurnal jet is responsible for the warming of the mixed-layer subregion between 10- and 20-m depth and, remarkably, this warming occurs over just a few hours in the late afternoon.

The sea-surface salinity (SSS) changes in the LES solely because of the entrainment of saltier water at depth through the stable halocline. Precipitation and evaporation are not included in the present model. The variability of SSS over a one-week period is shown in Fig. 9. On days 2-7, SSS increases only during the night (between 12:00 and 6:00 hrs). The amount of daily increase of SSS decreases over the week as the night-time MLD (Fig. 9b) increases and the salty halocline is located progressively further away from the surface. A fit to the MLD evolution leads to

$$\frac{dh}{dt} = 0.1 \frac{u_*^2}{N_0 h(t)} \,. \tag{19}$$

The coefficient of 0.1 in Eq. 19 for the deepening of the upper-ocean Ekman layer with an additional diurnally-modulated heat flux is about twice the coefficient in the entrainment law found by Pham and Sarkar [32] for the case without any heating. Thus, turbulence from the diurnal jet and night-time convection act over the 24-hr period to increase the entrainment rate.

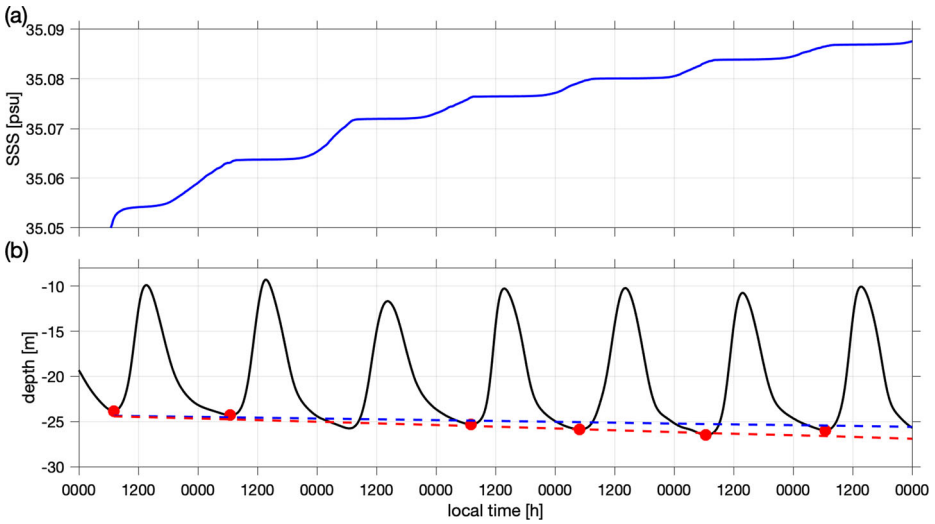

Fig. 9 Variability of sea surface salinity (SSS) and mixed-layer depth (MLD) due to turbulent entrainment at the base of the mixed layer: **a** SSS; and **b** MLD. Symbols in (**b**) denotes the maximum night-time MLD. Entrainment rate is estimated by a linear fit going through the nightly maximum MLD (red dashed line). The blue dashed line, which denotes the MLD in the case of no surface heat flux [32], is also shown for comparison

4 Equatorial Undercurrents

We turn to a problem, the Equatorial UnderCurrents (EUC), where subsurface shear of an ocean current combines with wind forcing and the diurnal cycle of heat flux to engender deep cycle (DC) turbulence that extends much deeper than the mixed layer and is modulated by the diurnal cycle. A striking feature of the mean flow observed in the EUC is that the gradient Richardson number ($Ri = N^2/S^2$) remains near the value 1/4 in the layer where DC turbulence is found. This suggests that the flow subject to DC turbulence is in marginal instability (MI) [34–36]. The deep cycle can be understood as a stratified shear layer in a state of marginal instability (MI) that is perturbed by some mechanism that varies diurnally. The identity of this diurnal trigger has been a subject of debate. Recent observational [35] and simulation [34] evidence identifies the daytime surface current as the trigger. During the day, solar radiation stratifies the uppermost few meters of the ocean, trapping the wind-driven turbulent momentum flux and allowing the acceleration of a strongly sheared surface current. After local noon, the stabilizing influence of solar heating relaxes, and in late afternoon, the surface current becomes unstable. Momentum from the surface current spreads downward, enhancing the shear in the MI layer, reducing Ri and thereby triggering strong turbulence. Countering this is turbulent mixing, which tends to mix the shear and stratification profiles so as to increase Ri, causing turbulence to decay. DC turbulence appears to be controlled by a combination of local shear and stratification (combining to produce the MI state) and surface fluxes of momentum and buoyancy (tipping the MI flow into the unstable regime each evening).

The results of this section are based on the those reported by Pham et al. [13] as well as additional results on the heat transfer. The initial conditions of the LES are chosen using the observations during the months of January, April, July and October. During these times,

measurement suggests considerable differences due to the seasonal variability in the MI state. There was variability in turbulence too, e.g the observed dissipation rates in April were low. It is of interest to examine how the DC turbulence would vary according to the difference in MI condition.

4.1 Numerical model

The governing equations are similar to the ones used in the previous section; however, the Coriolis term is suppressed and the evolution equation for salinity is omitted.

The subgrid stress, τ_{ij}, is modeled with a Smagorinsky-type model similar to Pham et al. [34] and the subgrid heat flux Q_j modeled with an assumption of unity subgrid Prandtl number. Surface boundary conditions are based on typical fluxes of momentum and heat observed at the sea surface. The momentum flux, τ_w, and the nonsolar heat flux, Q_{ns}, are constants equal to climatological monthly averages (see Table 2) and are applied as surface boundary conditions on velocity and temperature, respectively. The diurally-varing solar heat flux, $Q_{sw}(z,t)$, is applied as in the simulation of the diurnal warm layer discussed in the previous section. The maximum amplitude (most negative) of the solar flux at the surface, $Q_{s,max}$, is adjusted according to observational data. We take the observational data collected by the mooring deployed at $0°\ 140°W$ during the months of April, July, October and January from January 1979 to March 2013 and average them to obtain the surface fluxes that are listed in Table 2.

The LES model is initialized with mid-afternoon profiles of velocity and temperature representative of the target months. Each profile is the average of all observed values between 15:00 and 16:00 hours for the specified month during the period between September 1996 and November 2010. Mid-afternoon initialization is chosen to make the turbulence spin-up phase as natural as possible, since turbulence is typically weak at that time of day.

The computational domain is chosen to be 480 m by 80 m by 865m in the zonal, meridional and vertical directions, respectively, using 384 by 64 by 512 grid points. The horizontal grid spacing is 1.25 m. The vertical grid is uniform in the top 80 m with a spacing of 0.25 m. In the region below, a grid stretching of 3% is used with the largest spacing equal to 19 m at 865 m depth. Periodic conditions are used on the lateral boundaries and a sponge region is employed in the bottom 300 m. The domain dimensions are sufficiently large to capture the wavelength of the largest instability that is likely to arise.

Table 2 Parameters used in the simulated cases

Case	$\tau_w[Nm^{-2}]$	$Q_{s,max}[Wm^{-2}]$	$Q_{ns}[Wm^{-2}]$
Jan	–0.0681	–886.6	128.4
Apr	–0.0287	–879.9	106.8
Jul	–0.0612	–827.6	151.0
Oct	–0.0561	–936.2	126.3

$Q_{s,max}$ indicates the maximum value of surface solar radiation at noon. Q_{ns} is the non-solar part of the heat flux that includes long wave, latent and sensible heat fluxes and is generally a cooling flux

4.2 Results of equatorial undercurrents simulations

Simulations of the 3-day time period indicate that the DC turbulence occurs in all four simulated months. Thus, our initial observation-based inference that DC turbulence is absent in April must be modified; there is DC turbulence in April but limited to a thinner layer than in the other months as elaborated below and was therefore not clear in the moored observations of turbulence microstructure.

Figure 10 shows the enhanced dissipation rate which extends below the mixed layer depth (MLD) during night time. The turbulence in the DC layer can be stronger than the

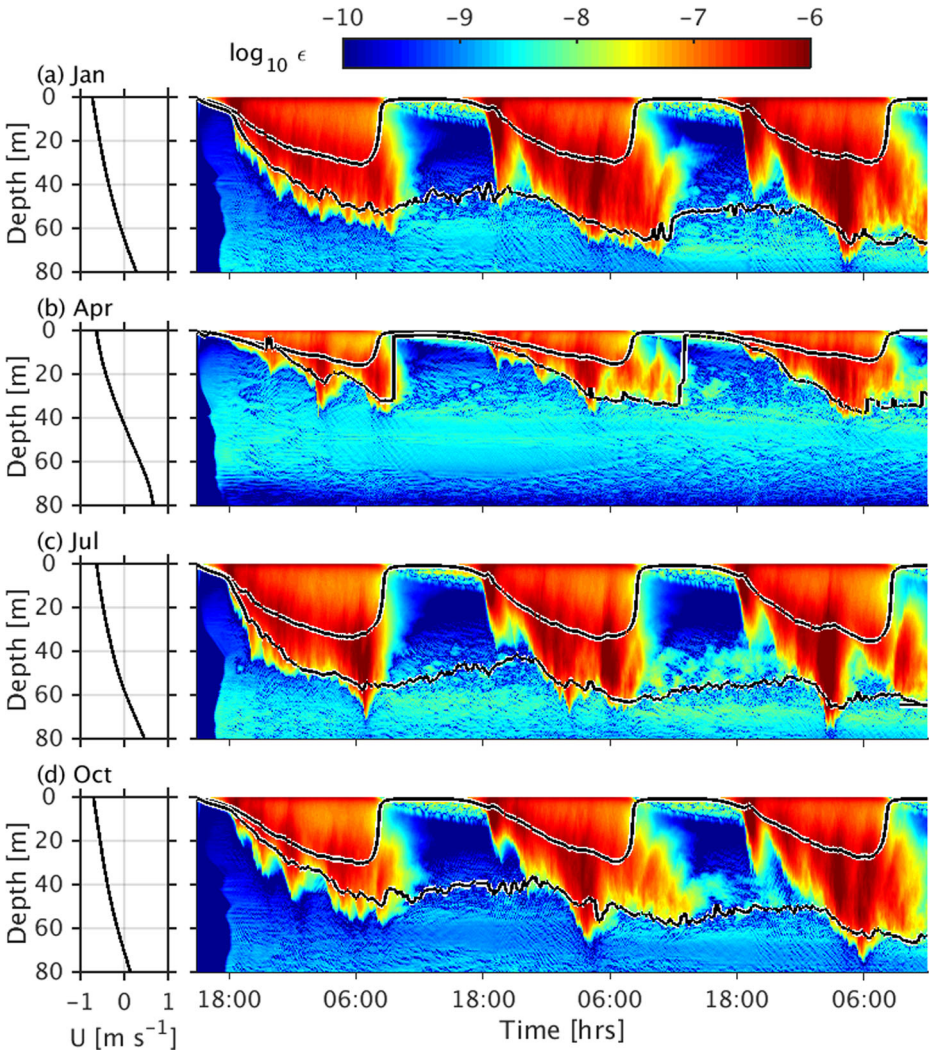

Fig. 10 Enhanced dissipation rate due to deep-cycle turbulence in the four simulations. Panels to the left show the profiles of zonal velocity at the initial time. The upper and lower solid lines on the dissipation panels mark the mixed layer depth and the MI depth where $Ri = 0.25$, respectively. At night time, strong turbulence extends up to 70-m depth in the months of Jan, July and October. The turbulence occurs at shallower depth in April due to the upwelling of the thermocline to 40-m depth

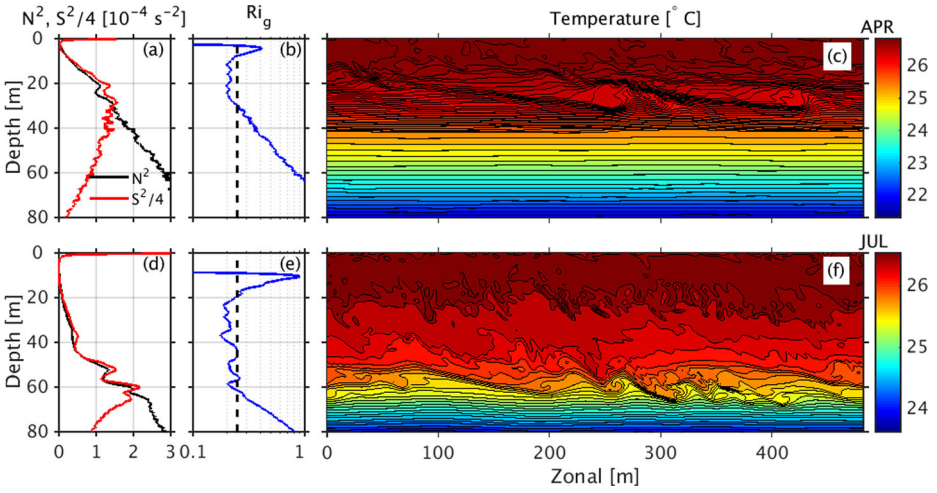

Fig. 11 Comparison of the structure of shear instabilities between the April simulation (**a, b, c**) and the July simulation (**d, e, f**). Cross-section shown at 2200 local time during the third night of the simulation. The instabilities are Kelvin-Helmholtz-type with 10-m overturns of isotherms

turbulence found in the mixed layer. The night-time DC turbulence occurs in distinctive bursts. The first burst of the night occurs consistently around 18:00 hours. In the late afternoon, as the solar radiation weakens, the wind-driven momentum trapped in the surface current is released and the shear becomes unstable. The resulting turbulent mixing generates a downward turbulent flux which triggers the shear instabilities in the DC layer. The subsequent turbulent bursts are as strong as the first burst and they extend deeper into the DC layer. Among the simulated cases, the April simulation has the shallowest DC turbulence due to the upwelling of the thermocline and the EUC jet during this time of the year. Both the shear and the stratification in the DC layer increases at the this time; however, the gradient Richardson number becomes significantly larger than 0.25. The flow loses its MI condition at depths where the three other cases have MI and, therefore, the DC turbulence does not extend as deep as in the other cases.

The difference between the DC turbulence in the April and July cases is illustrated in Fig. 11. The profiles of Ri in Fig. 11b, e clearly shows the difference in the MI condition. In the April simulation, due to the upwelling of the thermocline at this time of year, the stratification and shear rate at 30-m depth are considerably larger than that in the July simulation. As a result, Ri becomes larger than 0.25 at approximately 35-m depth and so the DC turbulence is capped at this depth. In contrast, subcritical Ri occurs down to 60-m depth in the July simulation, so the DC turbulence can extend to a greater depth. Despite the difference in the vertical extent, the intensity of DC turbulence is similar between the two cases. The turbulence in both cases are triggered by Kelvin-Helmholtz shear instability. The horizontal wavelength of the instability is longer in the April simulation suggesting the wavelength does not scale with the mixed layer depth but rather with the shear length scale local to the DC layer.

An important effect of DC turbulence is the heat flux it generates between the surface mixed layer and the underlying thermocline. The vertical gradient of the turbulent heat flux influences whether the water at specific depth warms or cools. Figure 12 contrasts turbulent heat flux Q_{turb} among the cases. At night, the heat flux exhibits one or more negative

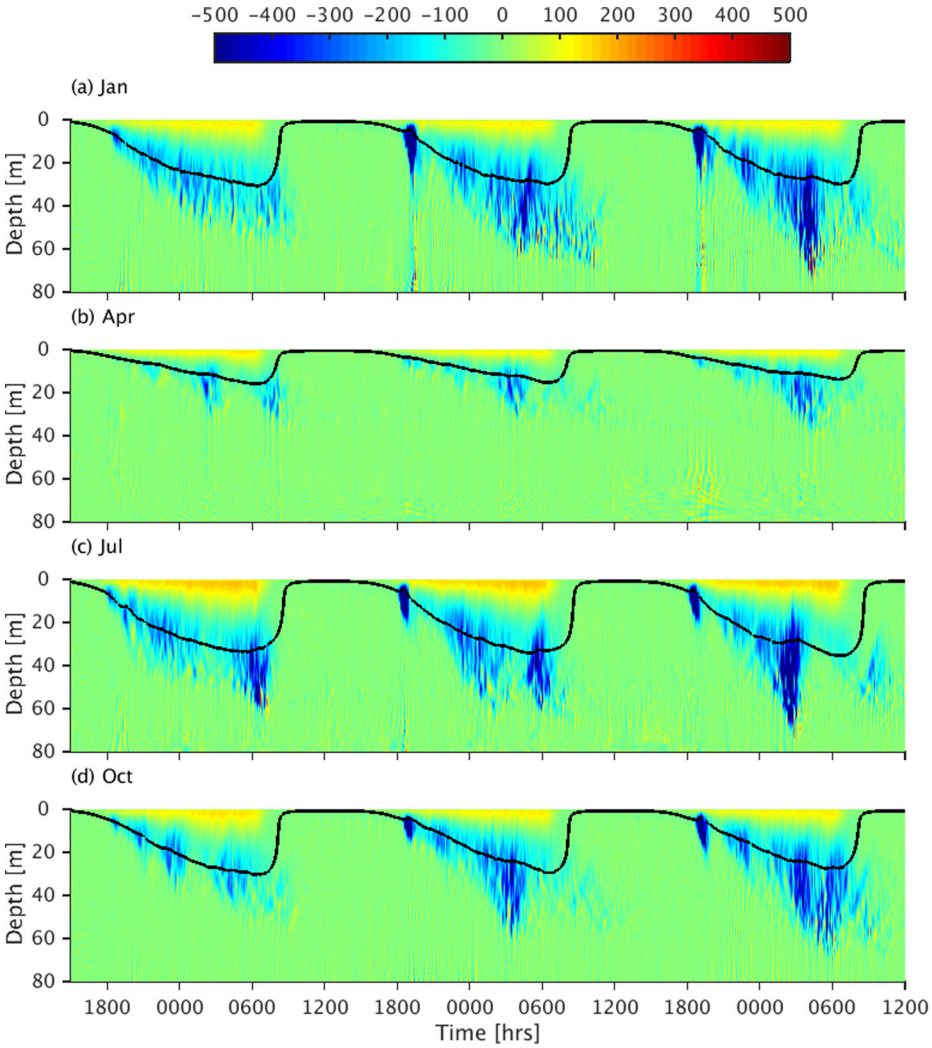

Fig. 12 Comparison of resolved turbulent heat flux, Q_{turb} in the four simulated cases. The amplitudes of the flux are similar between the cases but the vertical extent is shallower in the April simulation. Solid lines denote mixed layer depth

peak values in the MI layer, indicating a downward heat transport which often exceeds $500 W\, m^{-2}$ instantaneously. The vertical gradient is positive at depths above the peak and negative below. Therefore, DC turbulence cools the water in the mixed layer and warms the water in MI layer. DC turbulence reaches the greatest depths in the January, July and October simulations, with warming seen at 80 m depth (see Fig. 12). The April simulation has shallow MI layer, and thus warming only extends to 40 m depth. The night-time turbulent heat flux due to DC turbulence is more continuous in other seasons relative to the April simulation which shows a few distinct bursts of turbulent heat flux. The instantaneous peak values of turbulent heat flux are comparable among the simulations.

Table 3 Comparison of daily-averaged heat budget in the surface mixed layer

Case	$h_{MLD}\,[m]$	$Q_{surf}\,[Wm^{-2}]$	$J_q\,[Wm^{-2}]$	$\partial\hat{T}/\partial t\,[Kmonth^{-1}]$
Jan	30.5	–134	–96	0.8
Apr	16	–154	–79	3.0
Jul	33	–94	–96	0.0
Oct	31	–151	–60	1.9

h_{MLD} is the furthest distance from the surface that the mixed layer can reach over the day. Q_{surf} is the net heat flux that crosses the ocean surface. J_q is the daily-averaged resolved turbulent heat flux measured at h_{MLD}. $\partial\hat{T}/\partial t$ measures the rate of change of the temperature averaged over the mixed layer

How does the DC turbulence influence the temperature in the surface mixed layer on a daily basis? To answer this question, we analyze the daily-averaged heat budget in the mixed layer. The budget for the daily average can be described by the following equation:

$$\frac{\partial\hat{T}}{\partial t} = \frac{1}{h_{MLD}}\int_{-h_{MLD}}^{0}\frac{\partial T}{\partial t}dz = \frac{1}{\rho_0 c_p}\frac{\left(J_q - Q_{surf}\right)}{h_{MLD}}. \tag{20}$$

Table 3 compares the terms in the budget among the four simulations. Since the daily-averaged surface heat flux is negative in all simulations, its contribution to the budget is to increase the temperature of the mixed layer. In contrast, the turbulent heat flux cools the mixed layer from below. The difference between the surface heat flux and the turbulent heat flux (J_q) at the MLD location dictates whether there is a net increase or decrease in temperature. Among the simulations, the temperature increases faster in the April simulation while it does not change in the July simulation. In the April simulation, the surface warming flux ($-154\,\mathrm{Wm}^{-2}$) is larger in magnitude than the turbulent cooling flux ($-79\,\mathrm{Wm}^{-2}$). As a result, heat accumulates in the mixed layer. In contrast, the surface flux in the July simulation is relatively smaller ($-94\,\mathrm{Wm}^{-2}$) and the turbulent flux ($-96\,\mathrm{Wm}^{-2}$) at MLD are comparable so that the temperature does not change. The October and January simulations show intermediate values of warming between these two extremes. Thus, the intensity of the DC turbulence influences the temperature of the mixed layer. The stronger is the turbulence, the cooler is the temperature. Analysis of the TAO mooring data from 2006 to 2011 shows that the SST increases at a rate of 1.5 to 2.1 K per month during boreal spring while it decreases at a rate of 1.6 to 4.7 K per month during summer [12]. The present LES results are based on an average over a much longer period (1979-2013) that does not have the bias towards tropical instability waves seen in the 2006-2011 period but the larger SST increase in spring over summer in the LES is qualitatively consistent with these observational estimates [12].

5 Concluding Remarks

Turbulence is a crucial determinant of the upper-ocean thermal structure that modulates air-sea coupling and thereby weather and climate. Geophysical turbulence is often affected by variations in buoyancy, $b = -g(\rho_p - \rho_0)/\rho_0$, where ρ_p is the potential density and ρ_0 is the constant reference density. Three examples drawn from our recent work are discussed in the present paper to illustrate how wind, diurnal forcing and vertical buoyancy gradients interact to impact upper-ocean turbulence and mixing. Our tools are high-resolution DNS and LES.

In the first example of a shear layer in a uniformly stratified background, we discuss the lifecycle of the flow using DNS at relatively high Reynolds number (Re): transition to turbulence through a sequence of instabilities, thickening of the shear layer in the vertical, transport and mixing of the density field and, eventually, turbulence decay as the kinetic energy in the flow becomes insufficient to overcome the potential energy barrier (that increases with shear-layer thickening) to overturning, three-dimensional turbulent motions. Stratification, shear, turbulence, and terms in the turbulent kinetic energy budget exhibit qualitative differences as the flow evolves through different stages.

The second example concerns the diurnal warm layer (DWL) which forms as the upper-ocean boundary layer (OBL), that is driven by a wind stress (taken to be constant here), responds to the diurnal cycle of daytime solar insolation and night-time cooling. Daytime heating leads to increased near-surface stratification, the mixed layer thins to about 10 m, and the momentum input by the wind is trapped in a stratified, sheared layer at the surface, the so-called diurnal jet. In the evening, the stratification relaxes and there is a layer of descending shear that penetrates down to the capping halocline at 25 m. The diurnal jet and the descending shear are found to promote turbulence. The uptake of surface heat input by warming of the layer between 10- and 25-m depth occurs over a short period of about 4 hours in the late afternoon and evening as a result of the turbulent layer created by the descending shear.

The third example of the Equatorial Under Current (EUC) corresponds to a jet with asymmetric stratification and shear that is forced by the wind and a diurnal cycle of heat flux. LES is conducted for 4 different choices of initial conditions and surface forcing taken to represent the seasons. The simulations are able to capture not only the episodic nature of deep cycle (DC) turbulence and heat flux that is seen in the observations but also the seasonal variability of mixing. The local Richardson number, $Ri = N^2/S^2$, is the key parameter and the layer susceptible to DC turbulence is found to be in a state of marginal instability, $Ri \approx 0.25$. Wind, the diurnal cycle, and the initial conditions of shear and stratification influence the vertical and temporal variability of Ri which is the primary control on the formation and decay of DC turbulence. Accurate representation of the seasonal variability of turbulent mixing is found to be important for the seasonal variability of the warming/cooling trend of the EUC.

There are important upper-ocean turbulent processes that have not been considered here. The upper surface of the ocean is deformable. Surface waves affect upper-ocean mixing in mainly two ways: first, Stokes drift that leads to vertical transport by Langmuir cells and, second, wave breaking which leads to turbulence. It is worth noting that high-resolution simulations are leading to insights into surface wave-driven turbulence. We have not considered the influence of horizontal variability of the mean velocity and temperature in the present work. Submesoscale (100 m to 10 km horizontal scale) instabilities induced by lateral buoyancy gradients lead to complex profiles of vertical stratification that influence vertical OBL mixing and also lead to secondary turbulent flows. The interaction of lateral submesoscale variability with vertical mixing is a topic of ongoing research. The coupling of the OBL to the atmospheric boundary layer (ABL) is usually performed at coarse horizontal grid scales in numerical weather prediction. Coupled OBL-ABL process studies that resolve turbulence will become increasingly important to increase the fidelity of parameterized air-sea fluxes in regional and global climate models.

Acknowledgements We are pleased to acknowledge the support of NSF OCE-1355856, ONR N00014-17-1-2735 and NSF OCE-1851390.

Compliance with Ethical Standards

Conflict of interests The authors declare that they have no conflict of interest.

References

1. Peltier, W.R., Caulfield, C.P.: Mixing efficiency in stratified shear flows. Annu. Rev. Fluid. Mech. **35**, 135–167 (2003)
2. Smyth, W.D., Moum, J.N.: Length scales of turbulence in stably stratified mixing layers. Phys. Fluids. **12**(6), 1327–1342 (2000)
3. Pham, H.T., Sarkar, S., Brucker, K.A.: Dynamics of a stratified shear layer above a region of uniform stratification. J. Fluid. Mech. **630**, 191–223 (2009)
4. Pham, H.T., Sarkar, S.: Transport and mixing of density in a continuosly stratified shear layer. J. Turbulence. **11**, 1–23 (2010)
5. Brainerd, K.E., Gregg, M.C.: Diurnal restratification and turbulence in the oceanic surface mixed layer: 1. Observations. J. Geophys. Res. **98**, 22645–22656 (1993)
6. Callaghan, A.H., Ward, B., Vialard, J.: Influence of surface forcing on near-surface and mixing layer turbulence in the tropical Indian Ocean. Deep-Sea. Res. **I**(94), 107–123 (2014)
7. Moulin, A.J., Moum, J.N., Shroyer, E.L.: Evolution of turbulence in the diurnal warm layer. J. Phys. Oceanogr. **48**, 383–396 (2018)
8. Price, J.F., Weller, R.A., Pinkel, R.: Diurnal cycling: Observations and models of the upper ocean response to diurnal heating, cooling and wind mixing. J. Geophys. Res. **97**(C7), 8411–8427 (1986)
9. Sutherland, G., Marie, L., Reverdin, G., Christensen, K.H., Brostrom, G., Ward, B.: Enhanced turbulence associated with the diurnal jet in the ocean surface boundary layer. J. Phys. Oceanogr. **46**, 3051–3067 (2016)
10. Gregg, M.C., Peters, H., Wesson, J.C., Oakey, N.S., Shay, T.J.: Intensive measurements of turbulence and shear in the equatorial undercurrent. Nature **314**(14), 140–144 (1985)
11. Moum, J.N., Caldwell, D.R.: Local influences on shear flow turbulence in the equatorial ocean. Science **230**, 315–316 (1985)
12. Moum, J.N., Perlin, A., Nash, J.D., McPhaden, M.J.: Seasonal sea surface cooling in the equatorial Pacific cold tongue controlled by ocean mixing. Nature **500**, 64–67 (2013). https://doi.org/10.1038/nature12363
13. Pham, H.T., Smyth, W.D., Sarkar, S., Moum, J.N.: Seasonality of deep cycle turbulence in the eastern equatorial Pacific. J. Phys. Oceanogr. **47**, 2189–2209 (2017)
14. Hazel, P.: Numerical studies of the stability of inviscid stratified shear flows. J. Fluid. Mech. **51**, 39–61 (1972)
15. Miles, J.W.: On the stability of heterogeneous shear flows. J. Fluid. Mech. **10**, 496–508 (1961)
16. Mashayek, A., Peltier, W.R.: The 'zoo' of secondary instabilities precursory to stratified shear flow transition. Part 1 shear aligned convection, pairing, and braid instabilities. J. Fluid. Mech. **708**, 5–44 (2012)
17. Watanabe, T., Riley, J.J., Nagata, K., Onishi, R., Matsuda, K.: A localized turbulent mixing layer in a uniformly stratified environment. J. Fluid. Mech. **849**, 245–276 (2018)
18. Brucker, K., Sarkar, S.: Evolution of an initially turbulent stratified shear layer. Phys. Fluids. **19**, 101105 (2007)
19. Winters, K.B., Lombard, P.N., RJ, J., D'Asaro, E.A.: Available potential energy and mixing in density-stratified fluids. J. Fluid. Mech. **289**, 115–128 (1995)
20. Gregg, M.C., D'Asaro, E.A., Riley, J.J., Kunze, E.: Mixing efficiency in the ocean. Ann. Rev. Mar. Sci. **10**, 443–473 (2018)
21. Oakey, N.: Statistics of mixing parameters in the upper ocean during JASIN phase 2. J. Phys. Oceanogr. **15**, 1662–1675 (1985)
22. Osborn, T.: Estimates of the local rate of vertical diffusion from dissipation measurements. J. Phys. Oceanogr. **10**, 80–89 (1980)
23. Mashayek, A., Peltier, W.R.: Shear-induced mixing in geophysical flows: Does the route to turbulence matter to its efficiency? J. Fluid. Mech. **725**, 216–261 (2013)
24. Salehipour, H., Caulfield, C.P., Peltier, W.R.: Turbulent mixing due to the Holmboe wave instability at high Reynolds number. J. Fluid. Mech. **803**, 591–621 (2016)
25. Smyth, W.D., Moum, J.N., Caldwell, D.R.: The efficiency of mixing in turbulent patches: Inferences from direct simulations and microstrucure observations. J. Phys. Oceanogr. **31**, 1969–1992 (2001)

26. Salehipour, H., Peltier, W.R., Mashayek, A.: Turbulent diapycnal mixing in stratified shear flows: the influence of Prandtl number on mixing efficiency and transition at high Reynolds number. J. Fluid. Mech. **773**, 178–223 (2015)
27. Kaminski, A.K., Smyth, W.D.: Stratified shear instability in a field of pre-existing turbulence. J. Fluid. Mech. **862**, 639–658 (2019)
28. Paulson, C.A., Simpson, J.J.: The temperature difference across the cool skin of the ocean. J. Geophys. Res. **86**(C11), 11044–11054 (1981)
29. Jerlov, N.G.: Marine optics. Elsevier (1976)
30. Ducros, F., Comte, P., Lesieur, M.: Large-eddy simulation of transition to turbulence in a boundary layer developing spatially over a flat plate. J. Fluid Mech. **326**(1–36), https://doi.org/10.1017/S0022112096008221 (1996)
31. Pollard, R.T., Rhines, P.B., Thompson, R.O.: The deepening of the wind-mixed layer. Geophys. Astrophys. Fluid. Dynamics. **4**(1), 381–404 (1972). https://doi.org/10.1080/03091927208236105
32. Pham, H.T., Sarkar, S.: Turbulent entrainment in a strongly stratified barrier layer. J. Geophys. Res. Oceans **122**, 5075–5087 (2017). https://doi.org/10.1002/2016JC012357
33. Jonker, H.J.J., van Reeuwijk, M., Sullivan, P.P., Patton, E.G.: On the scaling of shear-driven entrainment: A DNS study. J. Fluid. Mech. **732**, 150–165 (2013)
34. Pham, H.T., Sarkar, S., Winters, K.B.: Large-eddy simulation of deep-cycle turbulence in an Equatorial Undercurrent model. J. Phys. Oceanogr. **43**, 2169–2184 (2013)
35. Smyth, W.D., Moum, J.N.: Marginal instability and deep cycle turbulence in the eastern equatorial Pacific Ocean. Geophys. Res. Lett. **40**, 6181–6185 (2013)
36. Thorpe, S., Liu, Z.: Marginal instability? J. Phys. Oceanogr. **39**, 2373–2381 (2009)